NANO: Brief Reports and Reviews
Vol. 4, No. 4 (2009) 201–216

World Scientific
www.worldscientific.com

MODELING OF PLASMONIC PHENOMENA IN NANOSTRUCTURED SURFACES

RODOLFO CORTES* and VÍCTOR COELLO
Centro de Investigación Científica y de Educación Superior de Ensenada
Unidad Monterrey, Alianza Sur No. 105
Nueva Carretera Aeropuerto Km 9.5 Parque de Investigación e
Innovación Tecnológica (PIIT), Apodaca
C. P. 66629, N. L. Mexico
**rcortes@cicese.mx*

Received 1 June 2009
Revised 24 June 2009

Plasmonic phenomena in nanostructured surfaces are modeled by considering isotropic point-like nanoparticles whose responses to an incident surface plasmon polariton (SPP) field are phenomenologically related to their effective polarizabilities. Numerical simulations of different SPP elastic (in-plane) scattering orders and the operation of simple plasmonic devices are presented. Futhermore, nonlinear microscopy with a tightly focused laser beam scanning over a sample surface was modeled by using of analytic representations of the Green dyadic in the near- and far-field regions, with the latter being approximated by the part describing the scattering via excitation of SPPs. In general, the stability with respect to geometrical parameters and dispersion were the main features investigated in the presented plasmonic phenomena.

Keywords: Surface plasmon polariton; nanostructured surfaces; plasmonic.

1. Introduction

Plasmonics is a novel area in optics that deals with surface plasmon polaritons (SPPs). SPPs are electromagnetic excitations coupled to electron plasma oscillations, which have the property of propagating along a metal–dielectric interface as quasi two-dimensional interface waves.[1] Nowadays plasmonic investigations are showing results that are of interest from the theoretical point of view, and that potentially have further technological applications, e.g., in miniaturization of photonic circuits with length-scales much smaller than currently achievable, inter-chip and intra-chip applications, in computer systems, and bio/sensor-systems.[2–4]

Considering the SPP interaction with and manipulation by arrays of surface scatterers,[5–16] extensive theoretical studies have been conducted. The problem is not trivial, since even a simple case as the single elastic (in-plane) SPP scattering by an individual nanoparticle placed on a metallic surface requires important computational resources and elaborate algorithms.[17] Experimental work has demonstrated that the elastic SPP scattering can be considered to be approximately isotropic.[18,19] Isotropic particles have also been pointed out as a limiting case of small (nano) particles in a rigorous consideration of SPP scattering,[17] and used in rather simplified simulations of SPP excitation with individual surface defects.[20] Bearing this in mind, one can approximate an elastically scattered SPP by a cylindrical SPP, which is described by the Hankel function with the lowest angular number

($m = 0$) and with the wavenumber determined by the same dispersion relation as for a plane SPP.[21] Thereby, the complicated mathematical treatment involved in the problem of SPP scattering by surface inhomogeneities is, up to some extent, considerably reduced. In this context, a relative simple scalar multiple scattering approach was used for simulation of SPP micro-components[22] and photonic bandgap structures[23] formed by a set of dipolar (nanosized) scatterers. Here, certain limitations on the accuracy of numerical results should be borne in mind.[24] For example, the effective polarizability of an individual scatterer is a phenomenological quantity that is difficult to relate to scatterer parameters such as size, susceptibility, etc. On the other hand, using the dipole scattering approach, a theory for light scattering from a random array of nanoparticles, spaced much less than an optical wavelength, was developed.[25]

In this work, the authors deal with the randomness in particle positions by convolving the single-particle Green's dyadic with a correlation function that describes the average properties of the particle distribution.[25] Furthermore, an approach based on the RLC circuit analogy was developed to produce analytical values for electromagnetic field enhancements within nanoarrays.[26] Lately, the scalar approach of Ref. 18 has been extended into a vectorial dipolar model for SPP multiple scattering[24] and used to calculate SPP scattering produced by band-gap structures[24] and model the operation of a micro-optical SPP interferometer.[27] Recently, this model was further developed[28] and applied to the problem of SPP guiding by chains of strongly interacting nanoparticles.[29] The developed model is based on the Green's function formalism and the dipole approximation for field scattering by nanoparticles. SPP modes also play a major role in surface enhancement phenomena as second harmonic generation (SHG). Enhanced second harmonic (SH) generation at rough metal surfaces has been the subject of numerous theoretical investigations concerned mainly with the angular distribution of far-field SH radiation.[30] Theoretical modeling of SH-scanning optical microscopy (SH-SOM) of nanostructures is quite a challenge in itself, because one has to deal with two coupled problems of multiple light scattering, i.e., one has to find self-consistent fields at both FH and SH frequencies. In this context, nonlinear microscopy of localized field enhancements in random metal nanostructures was modeled by using analytic representations of dyadic in the near- and far-field regions, with the latter being approximated by the part describing the via excitation of surface plasmon polaritons.[31]

A microscopic self-consistent approach to this problem developed by using the generalized Green dyadic is quite complicated and can be applied only to a very limited number of scatterers. Here, we present an overview of some of the problems, developments, and current progress related with our research in the modeling of plasmonic phenomena in nanostructured surfaces. We begin with an introduction to SPPs in Sec. 2, followed by a description of a scalar multiple scattering model in Sec. 3. In Sec. 4, the scalar approach was used for simulations on single- and multiple-SPP scattering in metallic surfaces. In Sec. 5, the above-mentioned model was extended into a vectorial dipolar model. Thus, the operation of a plasmonic interferometer that comprises an SPP beam-splitter formed by equivalent scatterers lined up and equally spaced was analyzed in Sec. 6. The possibility of simultaneous SPP excitation and in-plane manipulation with a square-lattice array of nanoparticles is presented in Sec. 7. A further developed approach was used, in Sec. 8, for simulating SH-SOM of metal periodic nanoarrays placed on metal surfaces with the SPP contribution to multiple scattering being taken into account. Finally, in Sec. 9, the main results of this work are outlined.

2. Surface Plasmon Polaritons

SPPs are oscillations of surface electron charge density that can exist at a metal/dielectric interface (Fig. 1). Associated with them, there exists an electromagnetic field that propagates along the interface, exhibiting exponential decays perpendicular to it. Therefore, SPPs show a high sensitivity to

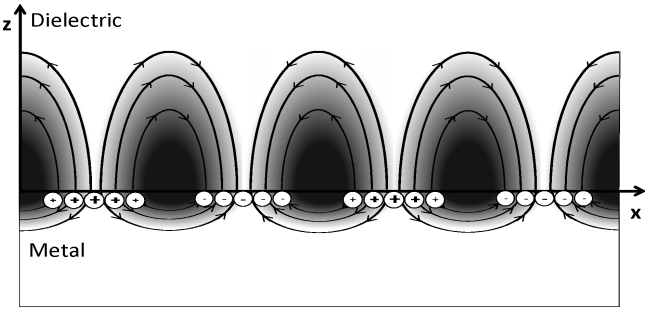

Fig. 1. Schematic representation of a SPP-electromagnetic field that exists at a metal/dielectric interface (XZ plane).

surface properties such as roughness and surface adsorbates.[1] As it is characteristic for evanescent fields,[32] for the SPP to exist, the wave number associated with it must be larger (in absolute value) than the light wave number in the neighbor media. SPP obey Maxwell's equations and they represent (quasi) two-dimensional waves. The electromagnetic derivation of the SPP modes results in the fact that such modes are possible only for p-polarization of light (TM-waves), since s-polarized waves (TE) do not satisfy the boundary conditions. Owing to their electromagnetic nature, it is not difficult to infer that SPPs can diffract, reflect, and interfere. Those properties are clearly exhibited in the course of SPP scattering.

Scattering of SPPs is usually caused by randomly placed surface imperfections (as even the most carefully prepared surfaces are not completely flat). Hereafter, we should distinguish between two kinds of SPP scattering: inelastic and elastic SPP scattering. For inelastic scattering, we will consider propagating field components scattered away from the surface decreasing the total energy stored in SPPs. Elastic scattering occurs when SPPs are scattered by surface imperfections along the surface plane, i.e., into other SPPs preserving the total SPP energy.

Concerning the mechanisms for SPP excitation, two techniques have been extensively developed: excitation by means of light and excitation by means of electrons. SPP excitation by electrons is beyond the scope of this work (an overview can be found in Ref. 1). Otto and Kretschmann configurations[1] are the mechanism most widely used for SPP excitation by light. They include a dielectric–metal–air system, in which a light beam is impinging on the metallic surface under an angle larger than the *critical angle*. The excitation occurs at the interface between air and metal and is recognized as a minimum in the angular dependence of the reflected beam power. An angular spectra analysis of SPP excitation allows one to deduce the SPPs characteristics, whose knowledge is indispensable for any kind of SPPs studies.

2.1. *Surface polaritons properties*

In order to show the SPP characteristics, first let us consider the interface between two semi-infinite media as air–metal. The SPP electric field existing in such a system (Fig. 1) can be represented as:

$$E(x, y) = E_0 e^{i\beta\cdot\hat{x}} \cdot e^{\gamma\cdot\hat{z}}\,, \tag{1}$$

which is an electromagnetic mode propagating in the x-direction along the surface and with an exponential decay perpendicular (z-direction) to it (Fig. 1). The SPP wave vector, β, and the air decay constant, γ, are derived through the use of Maxwell's equations and the boundary conditions, yielding the expressions:

$$\beta = \frac{2\pi}{\lambda_0}\sqrt{\frac{\varepsilon_m}{\varepsilon_m + 1}}\,, \quad \gamma = \sqrt{\beta^2 - k_0^2}\,, \tag{2}$$

being λ_0 the incident wavelength, ε_m the dielectric constant of metal, and k_0 the incident wave number. The SPPs modes have an exponential decay into each of the media, being then the SPP decay constant, γ_m, in the metallic medium given by:

$$\gamma_m = -\sqrt{\beta^2 - \varepsilon_m k_0^2}\,. \tag{3}$$

Other important SPP characteristics are the *SPP wavelength*,

$$\Lambda_{\mathrm{SPP}} = \frac{2\pi}{\beta}\,, \tag{4}$$

the *propagation length*, i.e., the length at which the intensity decreases to $1/e$ (along the surface),

$$L_{\mathrm{SPP}} = \frac{1}{2\beta_{im}}\,, \tag{5}$$

with β_{im} being the imaginary part of β, and *the penetration depth*, i.e., the length (perpendicular to the surface) at which the field amplitude decrease to $1/e$, that is given by:

$$d_1 = \frac{1}{\gamma_{(\mathrm{air})}}, \quad d_2 = \frac{1}{\gamma_{m_{(\mathrm{metal})}}}\,. \tag{6}$$

3. SPP Scalar Multiple Scattering Model

Typically, elastic scattering of SPP and related plasmonic phenomena (e.g., weak and strong localization) have been investigated by direct evaluation of the near-field optical image obtained at the place where the SPP is being resonantly excited.[33] This task could be numerically well-complemented by using a SPP scalar multiple scattering model. Such model is based on two assumptions:

(i) The elastic SPP scattering is dominant with respect to the inelastic scattering.
(ii) The SPP scattered by each scatterer represents an isotropic cylindrical SPP.

These assumptions allow one to avoid some of the complicated mathematical treatments involved in the problem of SPP scattering by surface inhomogeneities.[17] The field at a point in the plane pointed at by the vector $\mathbf{r}$ is given by:

$$E(\mathbf{r}) = E_0(\mathbf{r}) + \sum_{j=1}^{N} \alpha_j E(\mathbf{r}_j) G(\mathbf{r}, \mathbf{r}_j)\,, \qquad (7)$$

where $E_0(\mathbf{r})$ is the incident field, α_j is the effective polarizability of the jth dipole, $E(\mathbf{r}_j)$ is the self-consistent field at the site of the jth dipole, $G(\mathbf{r}, \mathbf{r}_j)$ is the field propagator, describing the scattered propagation of the scattered field from the jth dipole located at the source point $\mathbf{r}_j$ to the observation point $\mathbf{r}$. The self-consistent field to each dipole $E(\mathbf{r}_j)$ can be determined as:

$$E(\mathbf{r}_j) = E_0(\mathbf{r}_j) + \sum_{l=1, l\neq j}^{N} \alpha_l E_l(\mathbf{r}_j) G(\mathbf{r}_j, \mathbf{r}_l)\,. \qquad (8)$$

The total field at the site of the dipole j is the incoming field at the site of the scatterer and the sum of the scattered fields from all dipoles surrounding dipole j. The field in Eq. (8) then has to be inserted into Eq. (7) to find the total field at a point in the plane. The field propagator is given as:

$$G(\mathbf{r}, \mathbf{r}_j) = \frac{1}{4} H_0^{(1)}(\beta|\mathbf{r} - \mathbf{r}_j|)\,, \qquad (9)$$

where $H_0^{(1)}$ is the zero-order Hankel function of first kind and β is the propagation constant for the SPPs given by Eq. (2). The Hankel function of first kind of order n is defined as:

$$\begin{aligned} &H_0^{(1)}(\beta|\mathbf{r} - \mathbf{r}_j|) \\ &\quad = J_n(\beta|\mathbf{r} - \mathbf{r}_j|) + iY_n(\beta|\mathbf{r} - \mathbf{r}_j|) \\ &\quad = J_n(\beta|\mathbf{r} - \mathbf{r}_j|) \\ &\qquad + i\frac{J_n(\beta|\mathbf{r} - \mathbf{r}_j|\cos(n\pi)) - J_{-n}(\beta|\mathbf{r} - \mathbf{r}_j|)}{\sin(n\pi)}\,, \end{aligned} \qquad (10)$$

where $J_n(\beta|\mathbf{r} - \mathbf{r}_j|)$ is the Bessel function of the first kind and $Y_n(\beta|\mathbf{r} - \mathbf{r}_j|)$ is the Bessel function of the second kind, and n is the order. Often it is appropriate and easier to use the far-field approximation for the Hankel function. The far-field corresponds to large values of the argument, and the far-field approximation reads for large arguments[21]:

$$H_0^{(1)}(\beta|\mathbf{r} - \mathbf{r}_j|) \approx \sqrt{\frac{2}{\pi}} e^{-i(\pi/4)} \frac{e^{i\beta|\mathbf{r} - \mathbf{r}_j|}}{\sqrt{\beta|\mathbf{r} - \mathbf{r}_j|}}\,. \qquad (11)$$

The estimation of the magnitude of α, the effective polarizability of the individual scatterers has been done by fitting α such that the calculated (parabolic) interference pattern generated by an individual scatterer has the same contrast of an experimental (near-field) intensity distribution generated in analog form.[22] Thus, $\alpha = 3$ was a typical value that was used in the calculations. The SPP elastically scattered has been simulated by using a light wavelength $\lambda = 633\,\text{nm}$ and a dielectric constant $\varepsilon = -16 + i$ which corresponds to a silver film at the wavelength of illumination. The calculated total elastic cross-section of the scatterer (with $\alpha = 3$) was found to be: $\sigma = 0.22\,\mu\text{m}$. The value of σ can be used as a check of the estimation of α, i.e., for a symmetric surface defect considered theoretically[22] the same cross-section would correspond (in the first Born approximation) to a scatterer of $0.1\,\mu$m of height and $0.7\,\mu$m of radius. These parameters are in good agreement with experimental ones.[19,34,35] As a first case, we have considered the scattering from a single-particle. The propagation constant for the SPPs is taken real, so no damping across the surface is presented. Since only a single-particle is included, there is no scattering contribution from neighbors, and Eq. (8) therefore reduces to the following:

$$E(\mathbf{r}_j) = E_0(\mathbf{r}_j). \qquad (12)$$

Now a plane wave of unit amplitude traveling from left to right is incident on the nanoparticle that is:

$$E_0(\mathbf{r}_j) = e^{i\beta x_j}. \qquad (13)$$

With the use of Eqs. (1) and (2), the far-field approximation for the Hankel function in Eqs. (11) and (13), the total field from a plane wave and spherical wave can be written:

$$E(\mathbf{r}) = e^{i\beta x} + \alpha e^{i\beta x_j} \cdot \frac{i}{4}\sqrt{\frac{2}{\pi}} e^{-i(\pi/4)} \frac{e^{i\beta|\mathbf{r} - \mathbf{r}_j|}}{\sqrt{\beta|\mathbf{r} - \mathbf{r}_j|}}\,. \qquad (14)$$

Leading right to the intensity:

$$\begin{aligned} I(\mathbf{r}) &= |E(\mathbf{r})|^2 \\ &= 1 + \frac{\alpha^2}{8\pi}(\beta|\mathbf{r} - \mathbf{r}_j|)^{-1} + \frac{\alpha}{2}\sqrt{\frac{2}{\pi}} \\ &\quad \times \sin\left(\beta(x - x_j) + \cdots + \frac{\pi}{4} - \beta|\mathbf{r} - \mathbf{r}_j|\right). \end{aligned} \qquad (15)$$

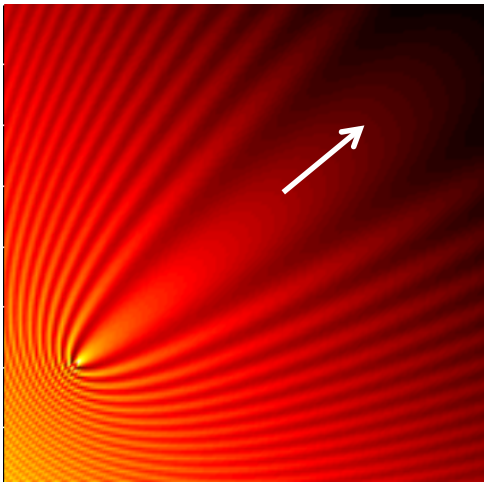

Fig. 2. Intensity distribution of a single-particle calculated with the scalar model. The illumination wavelength, $\lambda_0 = 750\,\text{nm}$ and the radius of the scatterer is $r = 50\,\text{nm}$. The white arrow indicates the SPP incident direction.

For maximum intensity, the sine oscillation has to equal 1, then:

$$\beta(x - x_j - \sqrt{(x - x_j)^2 + (y - y_j)^2}) + \frac{\pi}{4} = \frac{\pi}{2} + n2\pi\,, \tag{16}$$

where n is an integer. For the sake of simplicity, the position of the particle $r_j(x_j, y_j)$ is placed at the origo. Bearing this in mind and using β the SPP propagation constant from Eqs. (4) and (16) now reads for $n > 0$:

$$x\left(1 + \frac{1}{8n}\right) = \frac{y^2}{2n\Lambda_{\text{SPP}}} - \frac{n\Lambda_{\text{SPP}}}{2} - \frac{\Lambda_{\text{SPP}}}{8} - \frac{\Lambda_{\text{SPP}}}{128n}\,. \tag{17}$$

For growing values of n, the last term on the left hand side and the last two terms on the right hand side becomes vanishing compared the rest. Then, one can see that a parabolic fringes in y with a distance of $\Lambda_{\text{SPP}}/2$ between terms is expected. Figure 2 shows a simulation of Eq. (15) for a single-nanoparticle in a silver/air interface, where one can see that the fringes indeed have parabolic shape.

4. Single and Multiple SPP Scattering

Using the scalar model, single- and multiple-scattering regimes of SPP are elucidated. In a total area of $10 \times 5\,\mu\text{m}^2$, 50 nanoparticles have been randomly distributed in the left half. The particles

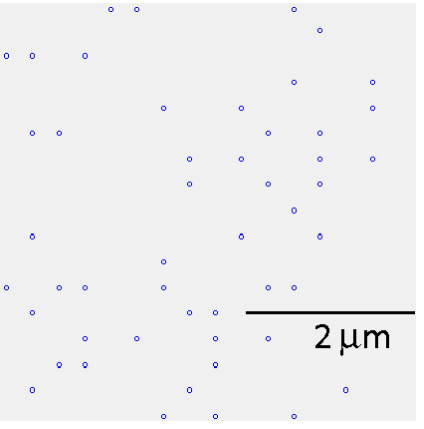

Fig. 3. Schematic representations ($5 \times 5\,\mu\text{m}^2$) of the nanoparticles distribution on a smooth gold-area.

placed on $5 \times 5\,\mu\text{m}^2$ smooth gold-area are chosen to have $\alpha = 3$ and their positions are depicted in Fig. 3 as circles with approximately true dimensions.

The particles were illuminated by a plane wave propagating from right to toward left (Fig. 4(a)). The corresponding propagation length, L, has a value of $\sim 23\,\mu\text{m}$, which is sufficiently large

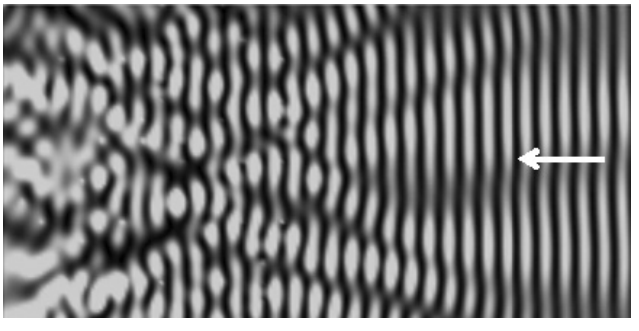

(a)

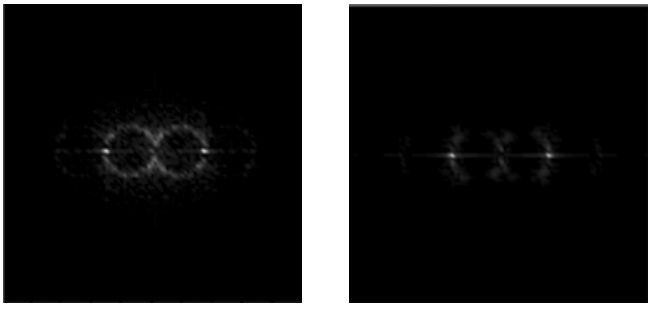

(b) (c)

Fig. 4. Gray scale representations of the total field intensity distribution (a) and the corresponding Fourier spectra (b) inside and (c) outside of the scatterers' area of Fig. 3. The intensity distribution within the area of $10 \times 5\,\mu\text{m}^2$ was calculated in the regime of single-scattering by 50 scatterers with $\alpha = 3$ randomly distributed in the left half. The white arrow indicates the SPP incident direction.

compared with the mean free path $l \sim R^2/\sigma \approx 4.5\,\mu$m and therefore one can simulate, in turn, both the single- and multiple-scattering regimes. The single-scattering regime is exhibited, in Fig. 4(a), as an interference pattern formed by the incident plane wave and the scattered cylindrical waves. We calculate a spatial Fourier spectrum in the area within which the nanoparticles were contained. The spectrum showed a pair of open circles with the radius corresponding to the propagation constant β (Fig. 4(b)). Outside of the nanoparticles area, a nearly plane reflected wave is propagating in the specular direction with respect to an imaginary boundary of the region of the particles. The corresponding Fourier spectrum contains two bright spots aligned along the perpendicular to this boundary (Fig. 4(c)).

Concerning the regime of multiple-scattering, the numerical simulations showed well-pronounced multiple interference effects (Fig. 5(a)). For example, optical fields of the waves scattered within the area of the nanoparticles are significantly stronger than those scattered outside of it. Actually the amplitude of those fields, in such area, is comparable with the amplitude of the incident optical field. We calculated the Fourier spectrum inside the area of the particles. The spectrum exhibited a nearly filled circle with a radius twice the propagation constant β (Fig. 5(b)). The corresponding spectrum outside of the particles' area showed a diffuse circle (Fig. 5(c)). Thus one can corroborate the existence of back-reflected waves in almost all possible directions and that are stronger than the wave speculary reflected (Fig. 5(a)).

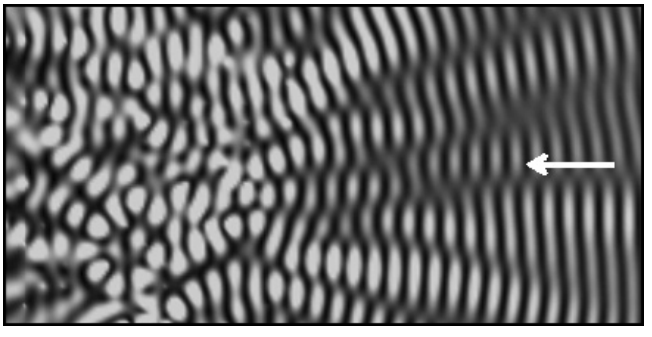

(a)

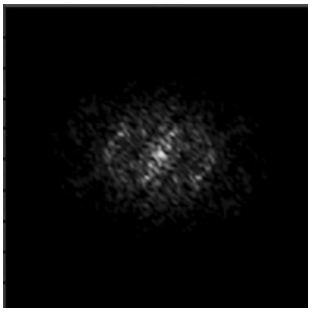

(b)

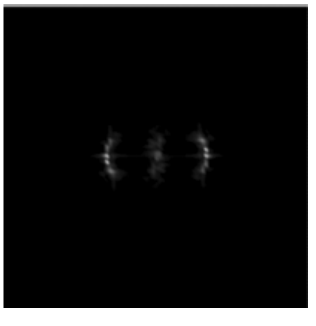

(c)

Fig. 5. Gray scale representations of the total field intensity distribution (a), that was calculated in the regime of multiple-scattering and the corresponding Fourier spectra (b) inside and (c) outside of the scatterers' area. All else as in Fig. 4. The white arrow indicates the SPP incident direction.

5. SPP Vectorial Multiple Scattering Model

Despite the apparent success, the scalar model presents limitations, one of them being that the effective polarizability of an individual scatterer is a phenomenological quantity which is difficult to relate to scatterer parameters such as size and dielectric susceptibility. The model was extended into a vector dipolar multiple-scattering theory and used, among other things, to calculate SPP scattering produced by band-gap structures.[24] The approach entails point-like dipolar scatterers interacting via SPPs so that the multiple-scattering problem in question can be explicitly formulated, making it very attractive for modeling of SPP plasmonic phenomena. The validity of the model was established for relatively large inter-particle distances, whereas for smaller distances, it was more accurate to use a total Green's tensor and include multipolar contributions in the scattered field (see Ref. 24 and references therein). The self-consistent polarization of each scatterer established in the process of multiple-scattering is obtained by solving the following equation:

$$\mathbf{P}_i = \alpha_i \cdot E^0(\mathbf{r}_i) + \frac{k_0^2}{\varepsilon_0} \sum_{n \neq i} \alpha_i \cdot G(\mathbf{r}_i, \mathbf{r}_n) \cdot \mathbf{P}_n \,, \quad (18)$$

where $\mathbf{P}_i$ is the polarization of the particle i, α is the polarizability tensor for particle i with the multiple scattering between the particle and the metal surface taken into account E^0 is an incoming electric field, $k_0$is the free space wave number, ε_0 is the vacuum permittivity and $G(\mathbf{r}_i, \mathbf{r}_n)$ is the Green's tensor for the reference structure (total field propagator). The Green's tensor G is the sum of a direct contribution G_d, in this case the free space Green's tensor, and an indirect contribution G_s that describes both reflection from the metal/dielectric interface and excitation of SPPs. The incoming E^0 describes

a Gaussian SPP field impinging on the arrangement of scatterers. For a spherical particle made of the same metal as the substrate, the polarizability tensor is given by:

$$\boldsymbol{\alpha} \approx \left[\mathbf{I} - \frac{\varepsilon-1}{\varepsilon+1}\frac{\varepsilon-1}{\varepsilon+2}\left(\frac{1}{8}\hat{x}\hat{x} + \frac{1}{8}\hat{y}\hat{y} + \frac{1}{4}\hat{z}\hat{z}\right)\right]^{-1} \cdot \boldsymbol{\alpha}^0 , \tag{19}$$

where $\mathbf{I}$ is the unit dyadic tensor, ε is the metal dielectric constant, $\hat{x}, \hat{y}, \hat{z}$ are unit vectors in a Cartesian coordinate system with $\hat{z}$ being perpendicular to the air–metal interface, and $\boldsymbol{\alpha}^0 = \varepsilon_0 \mathbf{I} 4\pi a^3(\varepsilon-1)/(\varepsilon+2)$ is the free space polarizability tensor in the long-wave electrostatic approximation with a being the sphere radius. The polarizations in Eq. (1) and the total field,

$$\mathbf{E}(\mathbf{r}) = \mathbf{E}^0(\mathbf{r}) + \frac{k_0^2}{\varepsilon_0}\sum_n \mathbf{G}(\mathbf{r}, \mathbf{r}_n) \cdot \mathbf{P}_n \tag{20}$$

can be calculated using the appropriate Green's tensor for the reference structure $G(\mathbf{r}, \mathbf{r}_n)$. Considering both the source and observation points being close to a meal surface but far away from each other, one can approximate the total Green dyadic (which includes the direct and indirect terms) with the part of the indirect Green dyadic concerned with the excitation of SPPs.[24] In this approximation, which is actually asymptotically correct as the in-plane separation of source and observation points increases towards infinity,[36] the Green dyadic can be represented by:

$$G_{\mathrm{SPP}}(r, r_n) \approx \alpha_{zz}(\lambda) e^{iK_z(z+h)} H_0^1(K_\rho \rho) * \left[\hat{z}\hat{z} + \cdots \right.$$
$$\left. (\hat{z}\hat{\rho} - \hat{\rho}\hat{z})\frac{K_z}{K_\rho} - \hat{\rho}\hat{\rho}\left(\frac{K_z}{K_\rho}\right)^2\right], \tag{21}$$

where H_0^1 is the zero-order Hankel function of the first kind, $\rho = |r_{II} - r'_{II}|$, $\hat{\rho} = (r_{II} - r'_{II})/\rho$, with II referring to the projection of the radius vector on the xy plane, which coincides with the metal–air interface, and z refers to the height of observation point r above the surface, while h refers to the height of the source point r'. Finally, K_ρ and K_z are the components of the three-dimensional SPP wave vector

$$K_\rho = k_0\sqrt{\frac{\varepsilon}{\varepsilon+1}}, \tag{22}$$

$$K_z = \sqrt{k_0^2 - K_\rho^2} \tag{23}$$

and

$$\alpha_{zz}(\lambda) = \frac{K_\rho}{2}\left(\sqrt{\varepsilon}\left(1 - \frac{1}{\varepsilon^2}\right)\frac{1+\varepsilon}{\varepsilon}\right)^{-1}. \tag{24}$$

The complete analysis of the validity domain of such an approximation is beyond the scope of this work and can be found elsewhere.[24]

5.1. *Multiline mirror*

As previously mentioned, a single circular nanoparticle is assumed to scatter light as cylindrical waves, so no preferred direction of scattering is presented. By placing particles in line of nanoarrays, a common plane wavefront of the scattered light can be achieved. From an application point of view, it seems obvious to exploit line arrays to reflect the wavefront to the applied field in order to make a mirror effect. The idea has been modeled for a line array of $3\,\mu$m length and whose inclination compared to the applied field is 45°.[22] The line arrays are far from being perfect mirrors since much of the incident light may pass through the structures. This fact can be compensated for by placing an array of lines that satisfy the Bragg condition, $2d\sin\theta = n\lambda$, where d is the separation distance, θ is the angle the beam makes with the mirror and n is a whole number. Here, we chose an inter-particle distance of 200 nm and an inter-line separation of 350 nm with an incident beam angle of 60°. The simulation has been performed with an incoming Gaussian beam of the form:

$$E_0 = e^{(-(y^2/w^2)+i\beta x)}. \tag{25}$$

The incoming wavelength, λ_0, the beam waist, w, and the particle radii, r, were fixed to 750 nm, $2\,\mu$m, and 60 nm, respectively. Figure 6 shows the mirroring effect from the nanoparticles. However, much of the signal is still transmitted. This fact is expected when only a few particles lines are used. With many layers of particles in an array, it is possible to obtain almost all of the reflected power with certain wavelengths of the incoming beam, that is the principle of the SPP band gap (SPPBG) structures. SPPBG phenomena are beyond the scope of this work but an overview can be found in Ref. 37.

Another plasmonic device, realizable by a certain array structure of nanoparticles, is a focusing micromirror. The concept is to place the particles along a parabolic curve $(y - y_0)^2 = 4F(x - x_0)$ where the coordinate (x_0, y_0) is located at the bottom of the mirror, F is the focal length and x is

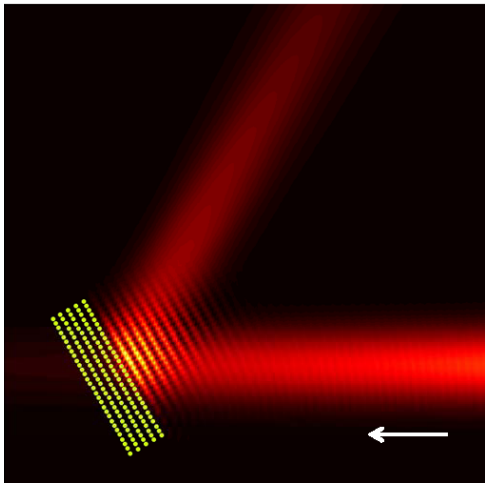

Fig. 6. Intensity distribution of a multiline mirror with five lines of 30 nanoparticles with radius $r = 63\,\text{nm}$ Inter-particle and inter-layer distances are 200 and 350 nm, respectively. The incoming SPP beam has a wavelength, $\lambda_0 = 750\,\text{nm}$. The white arrow indicates the SPP incident direction.

along the optical axis. In principle, this works for the two-dimensional case of SPP propagation in the same way as the three-dimensional case of a parabolic screen of a solar cooker, which concentrates reflected solar light at a cooking pot. Hence, at the point $(x_0 + F, y_0)$, a concentration of light is expected. In Fig. 7, we simulated a nanomirror with $F = 8\,\mu\text{m}$, where the focusing effect was clearly seen. For applications matters, focusing nanomirrors give the possibility to enhance SPP signal locally in a controllable way. One can think to exploit that feature in, for example, biosensors and surface-enhanced Raman spectroscopy.

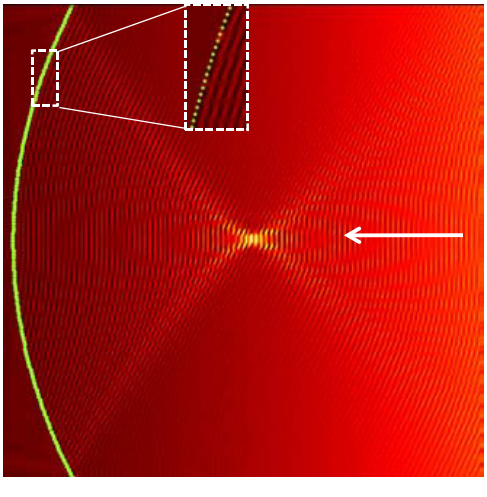

Fig. 7. Intensity distribution map in an area of $30 \times 30\,\mu\text{m}^2$ calculated for a curved micromirror with a focal length $F = 15\,\mu\text{m}$ and composed of 140 nanoparticles with inter-particle distance of 220 nm. The dotted line represents the curved nanomirror. All else as in Fig. 6.

6. Plasmonic Interferometer

Based on the configuration most suitable for realization of a 3-dB SPP beam-splitter, the feasibility of fabricating an SPP interferometer was corroborated. In order to numerically build step-by-step the interferometer, first, we investigated the in-plane scattered field created with a 5-μm-wide Gaussian SPP beam $\lambda = 750\,\text{nm}$ of unit amplitude impinging on an equally spaced line of nanoparticles which acts as a beam-splitter. Thus, it come out that, for a line of 200 nanoparticles with inter-particle distance of 280 nm and with particle radius of 64 nm, a nearly 50/50 beam splitter is realizable (Figs. 8(a) and 8(b)). The angle of incidence was set at $\theta_0 = 16°$. Note that these values match well to the experimentally reported ones[38] including equivalence in volume of the experimental cylindrical particle and the calculated spherical particle in our case. In the simulations, the incident SPP propagates from left to right and the dielectric constant used was $\varepsilon = -23.11 + 1.4i$ which corresponds to gold at 780 nm. The SPP interferometer has been completed by adding a second beam impinging at the incident angle of $-\theta_0$ (Figs. 9(a)–9(d)). The numerical simulations showed that the intensities of two output beams, which result from the interaction of the incident beams with the beam splitter, vary as a function of the introduced phase difference φ between the incident beams (Fig. 10) in a fashion that is very similar to the experimental results.[38] Deviations from the behavior expected in an ideal loss-less interferometer are related to the aforementioned problems with the energy conservation: the radius of 64 nm used in simulations was probably too large in this respect but just large enough to ensure the efficient operation of the beam-splitter and the interferometer.

7. Simultaneous SPP Excitation and Manipulation

In this section, using the vectorial dipolar model for multiple SPP scattering,[24,39,40] we investigate the possibility of simultaneous SPP excitation and propagation control with periodic square arrays of nanoparticles illuminated by a normally incident Gaussian beam. Following a step-by-step process, first we calculate the in-plane scattered field

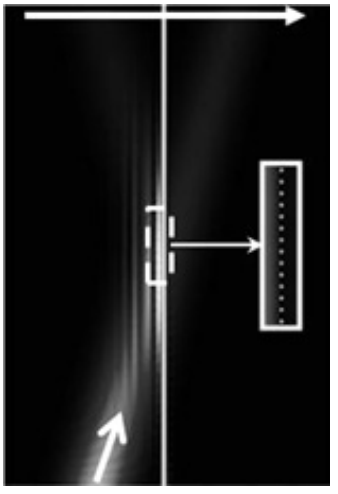

(a)

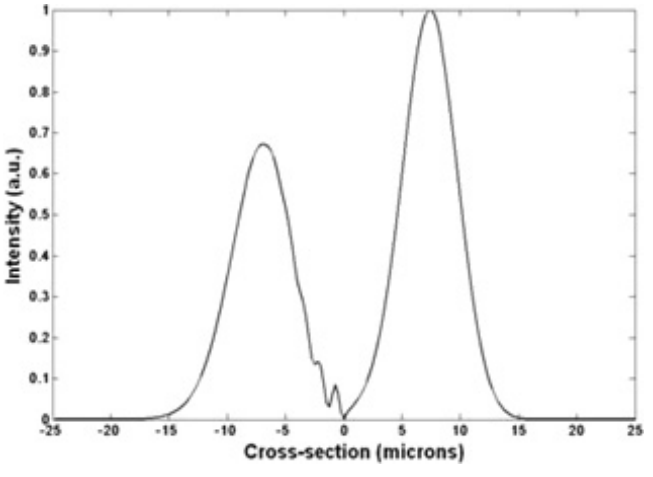

(b)

Fig. 8. Intensity distribution map in an area of $30 \times 50\,\mu\text{m}^2$ calculated for an SPP beam-splitter composed of 300 nanoparticles with the radius of 64 nm separated by 280 nm and for the light wavelength of 750 nm. The incident angle is set at 16° with regard to the line of particles. The dashed white arrow in (a) indicates the cross-section shown in (b) whereas the solid white arrow in (a) indicates the SPP incident direction. The dotted line represents the beam splitter.

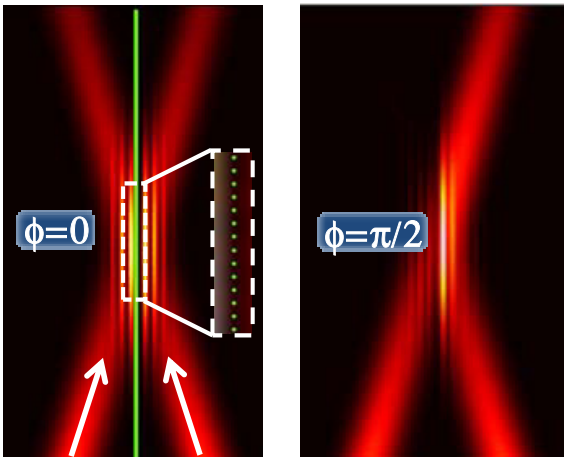

(a) (b)

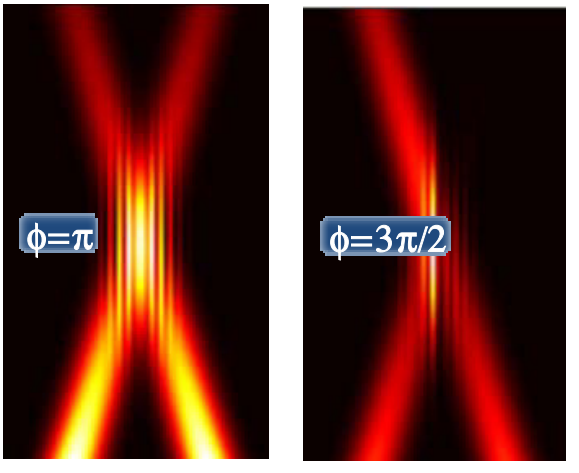

(c) (d)

Fig. 9. Intensity distribution map in an area of $30 \times 50\,\mu\text{m}^2$ calculated for an SPP interferometer with the parameters as in Fig. 8. The SPP maps have been calculated for the relative phase differences between the incident beams $\varphi =$ (a) 0, (b) $\pi/2$, (c) π, and (d) $3\pi/2$.

created by a normally incident Gaussian beam ($\lambda_0 = 750\,\text{nm}$, FWHM $= 5\,\mu\text{m}$, x-pol) of unit amplitude impinging on a 150 nm-period square lattice (width $w \approx 1.05\,\mu\text{m}$, length $L \approx 15\,\mu\text{m}$) of nanoparticles with radius, r, of 20 nm (Figs. 11(a)–11(c)). The entire system is simulated on a gold surface with dielectric constant $\varepsilon = -23.11 + 1.4i$. The configuration, in general, can be considered as fairly similar to experimental realized ones.[15,16] Figure 11(b) shows numerical simulations of a direct SPP excitation taking place at the lower (along y-axis) nanoarray edge. Hereafter, for all

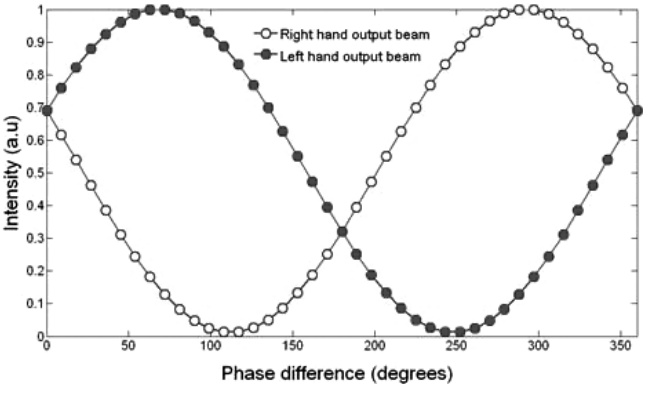

Fig. 10. Dependencies of the right and left hand output beam intensities of Fig. 9 as functions of the phase difference between the two input beams. All else as in Fig. 9.

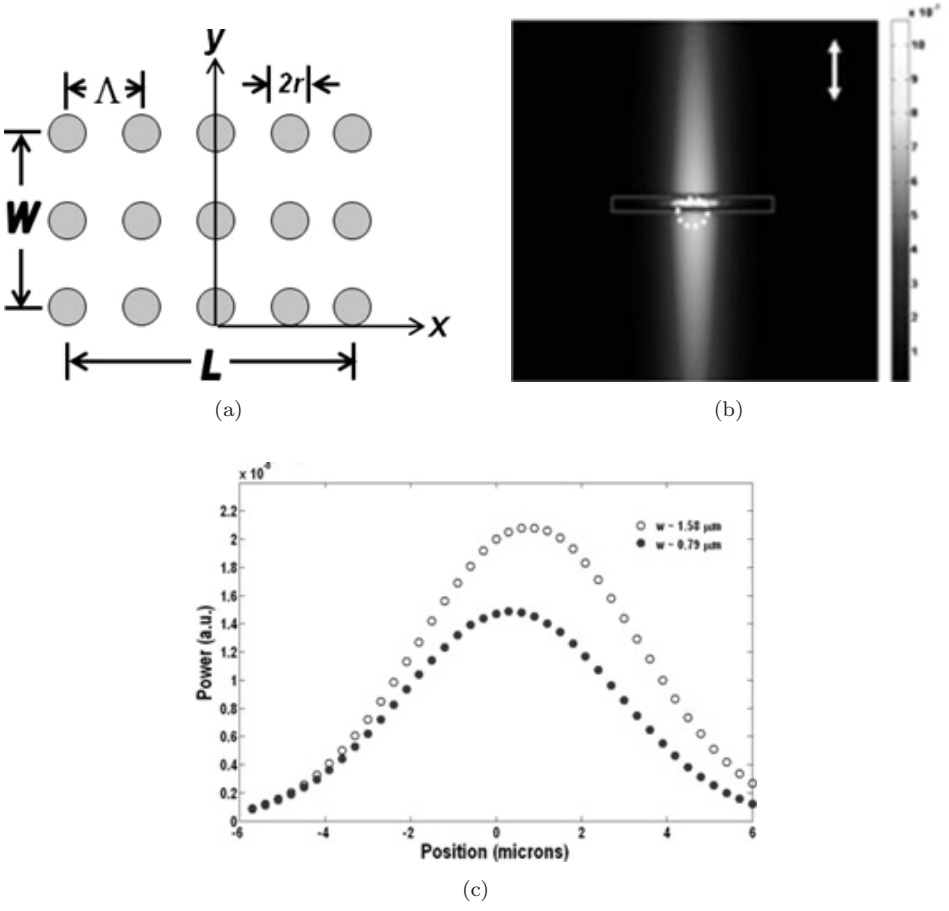

Fig. 11. Schematic layout of a periodic square-lattice gold nanoparticle array, where r is the particle radius, L, w, and Λ are the array length, width, and period, respectively. (b) Electric field magnitude distribution ($40 \times 40\,\mu\text{m}^2$) calculated at the height of 80 nm, above the air–gold interface for the incident (solid circle) Gaussian light beam (wavelength, $\lambda = 700$ nm, FWHM $= 5\,\mu$m, the polarization is along y-axis) being incident on the nanoarray (dotted square). The lateral size of the nanoarray is 175 nm. (c) The power of the SPP beam propagating in the positive direction of y-axis calculated as a function of the incident beam position (along the y-axis) for two array width w values. The arrow in (b) indicates the incident light polarization.

images in this section, the total field is calculated 80 nm above the air–gold interface, and the incident beam has been removed, i.e., only scattered SPP appear in the pictures. Figure 11(c) shows the power of the SPP beam propagating in the positive direction of y-axis calculated as a function of the incident beam position (along the y-axis). The calculations were made for two distinct w values. An asymmetric behavior was exhibited in both calculated curves. One can notice that once the incident beam is not in contact with the nanoarray, the optical power is weak (Fig. 11(c)); this is expected, considering that no SPP can be launched without interacting with the nanoarray. Once the launching of SPP is achieved, in this way, from an application point of view, one can exploit the nanoarrays in order to manipulate the SPP propagation. Scattering of the plasmons at nanoparticle arrays also enables guiding of the SPPs. A particularly simple geometry of a plasmonic device (waveguide) is presented in Figs. 12(a)–12(d). The waveguide consists of a periodic square-shaped nanoarray of $w \approx 2\,\mu$m and $L = 15\,\mu$m. We launched plasmons by illuminating with a normally incident Gaussian beam ($\lambda = 750$ nm, FWHM $= 2.5\,\mu$m, y-pol), either end of the nanoarray. The SPP waveguiding capability is evidenced by the SPP beam coming out of the waveguide (Figs. 12(a)–12(d)).

The wavelength dependence of the SPP waveguiding (Figs. 12(a)–12(d)) is understood because of the different SPP propagation lengths, Eq. (5).

SPP waveguiding is almost not observed when the incident beam is placed on the mid section of the nanoarray (Fig. 13).

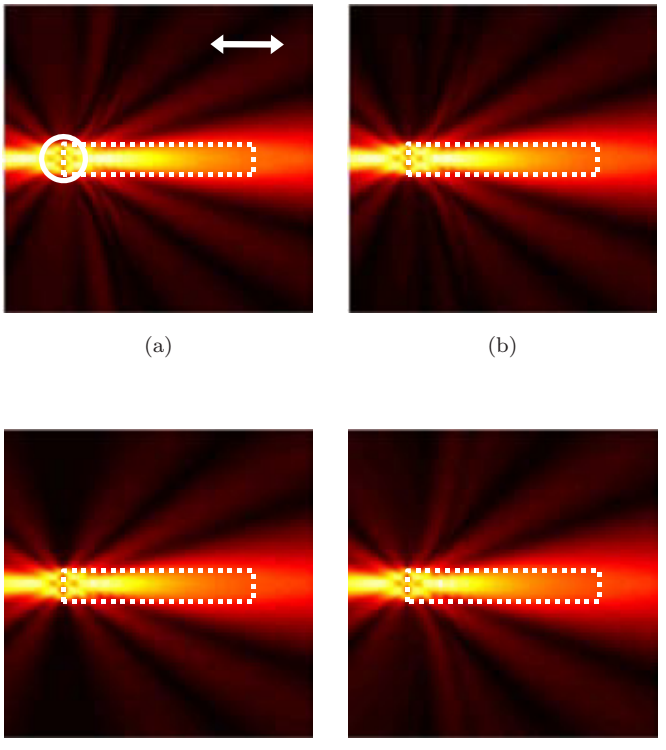

Fig. 12. Electric field magnitude distributions ($20 \times 20\,\mu m^2$) calculated for λ_0 = (a) 650, (b) 700, (c) 750, and (d) 800 nm using nanoarray waveguides with $L = 12\,\mu m$, $w = 2.5\,\mu m$, $r = 20$ nm, and $\Lambda = 200$ nm. The incident beam position for all images is placed at left entrance. The solid circle in (a) represents the incident Gaussian beam polarized along the waveguide array axis. The arrow indicates the incident light polarization in all cases.

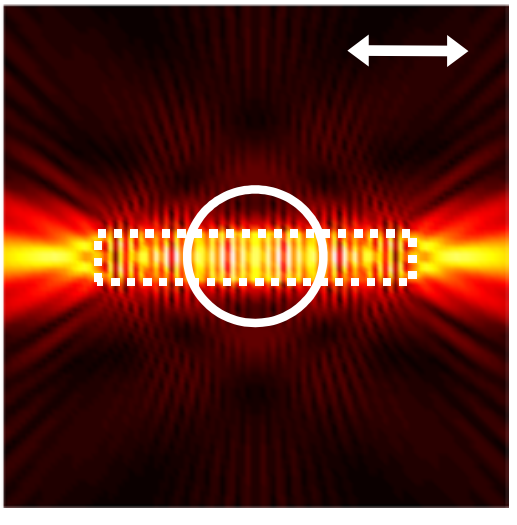

Fig. 13. Electric field magnitude distributions ($20 \times 20\,\mu m^2$) calculated for a nanoarray waveguide with and incident beam positions placed at the waveguide mid section and for $\lambda = 750$ nm. All else as in Fig. 12.

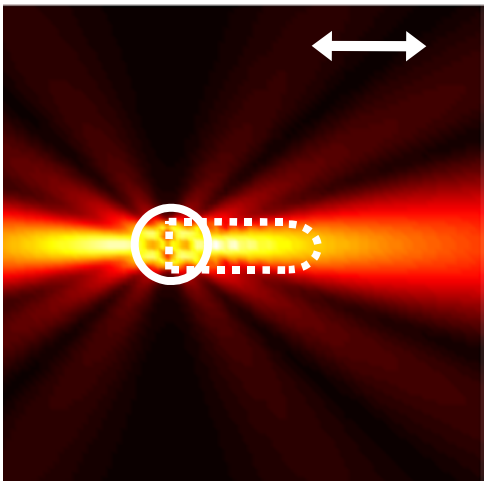

Fig. 14. Electric field magnitude distributions ($20 \times 20\,\mu m^2$) calculated for a nanoarray with semi-circular exit shape. The solid circle represents the incident Gaussian beam (polarized along the x-axis, FWHM = 2.5 μm), $\lambda_0 = 750$ nm, $r = 20$ nm, $L = 6\,\mu m$, $\Lambda = 200$ nm, and $w = 2\,\mu m$. The arrow indicates the incident light polarization in both cases. All else as in Fig. 1(b).

At the mid section, the nanoarray is almost symmetric over the extent of the incident beam and therefore cannot scatter efficiently in the axial direction since the incoming propagating vector and the propagating SPP vector are hardly matched. However, this symmetry is broken at the nanoarrays ends where light is scattered into propagating SPP modes. Likewise, propagating SPP modes are excited in thin-film surface utilizing gratings or dots. In analogy with light propagation in optical fibers, SPP propagation is not limited to symmetric-straight nanostructures. For example, a square-shaped nanoarray with a semicircumference exit (right end) can be proved for SPP focusing (Fig. 14).

8. Nonlinear Localized Field Enhancements

Novel optical phenomena arising from the propagation of SPPs at a weakly-corrugated metal surface originated original contributions in the area of SPP-enhancement of second harmonic (SH) diffraction.[41,42] With the variety of experimental results obtained in this context, it is rather important to understand the image formation process. Especially for systems like the curving microrings of organic molecules or enhancement effects from randomly positioned metal nanoparticles. Here,

an image formation model for SH microscopy is developed and used to simulate both first harmonic (FH) and SH optical images for a gold film covered with randomly distributed particles. This section treats SH-SOM of nanostructures, i.e., small spheres placed on a metal substrate, within the framework of the point-dipole approximation with the Green dyadic being approximated by analytic expressions available for the near- and far-field regions. While the near-field approximation is well known,[43] the far-field analytic expression is based on the recently established fact that, near a metal surface and for sufficiently large distances from a scattering source, the Green dyadic can be approximated by its part associated with the SPP excitation.[24] The modeling described in this section involves several intervening stages. First, the self-consistent FH field established in a scattering system is determined in relation to a position of a tightly focused scanning FH beam illuminating the sample. Secondly, the self-consistent SH field (driven by the self-consistent FH field) is found in the scattering system. Finally, thus determined (for each position of the incident beam) FH and SH field are used to calculate the corresponding field intensities at the site of a remote detector, resulting in FH and SH images.

8.1. *The self-consistent field*

The problem of multiple scattering in a system of nanoparticles, which are placed near a metal surface and illuminated by an incident electric field $E_0(\mathbf{r})$ at the wavelength λ, can be treated in the electric-dipole approximation, i.e., by treating each nanoparticle as a dipolar scatterer.[43] There, the Green dyadic approximation has showed to noticeably deviate from the exact total Green dyadic for small distances (less than a few wavelengths) between the source and observation points. On the other hand, its usage for simulations of the SPP bandgap structures consisting of nanoparticles arranged in a periodic pattern gave quite reasonable results even though the inter-particle distance was close to half of the wavelength.[24] However, for randomly placed nanoparticles with relatively high densities,[41,44] some particles are in or close to contact with each so that the inter-particle distances can be down to a small fraction of the wavelength, i.e., in the near-field domain. In such a case, one can take advantage of the near-field (electrostatic) approximation of the total Green dyadic that can be expressed in a simple analytic form[43]

$$G_{nf}(r, r', \omega) = D_{nf}(r, r', \omega) + I_{nf}(r, r', \omega)\,, \quad (26)$$

where $D_{nf}(r, r', \omega)$ is the direct part of the near-field propagator given by

$$D_{nf}(r, r', \omega) = -\frac{c^2}{4\pi\omega^2}\frac{3e_R e_R - I}{R^3} \quad (27)$$

with $R = |r - r'|$, $e_R = (r - r')/R$ and $\mathbf{I}$ being the unit tensor, while the indirect part $I_{nf}(r,\, r',\, \omega)$ of the near-field propagator, for the air–metal interface coinciding with the plane $z = 0$, can be expressed as

$$I_{nf}(r, r', \omega) = D_{nf}(r, r', \omega) * M(\omega) \quad (28)$$

with $r' = (x', y', -z')$ pointing to the position of the mirror image of the source point and

$$M(\omega) = \frac{\varepsilon - 1}{\varepsilon + 1}\begin{pmatrix} -1 & 0 & 0 \\ 0 & -1 & 0 \\ 0 & 0 & 1 \end{pmatrix}. \quad (29)$$

Both approximations considered above are limited to either short- or long-interaction distances. The main idea in this approach is to use the near-field dyadic (Eq. (26)) for distances longer than a certain (transition) distance related to a specified fraction of the light wavelength used in the particular simulations. A natural requirement to such a transition distance would then be that no apparent (unphysical) jumps should be seen in the dyadic components when switching from one expression to another one.

In order to find a proper distance for the transition between the two dyadics, the radial dependence of the nonzero dyadic components G_{zz}, G_{xx}, and $G_{zx} = G_{xz}$ were calculated using accordingly Eqs. (21) and (26) at different distances from the gold-surface and for different transition distances at the wavelength of $\lambda = 750\,\text{nm}$. Based on these calculations, the transition distance of $3\lambda/5$ is chosen (Fig. 15). It should be noted here that the near-field parts of components G_{zz}, G_{xx} are both one-order of magnitude larger than the remaining nonzero components $G_{zx} = G_{xz}$. Furthermore the real parts of these components are approximately one-order of magnitude larger than their imaginary parts. However, generally speaking, it is not possible to find the transition distance that would ensure smooth transitions for all dyadic components. For example, the transition of the G_{zz} components seems rather abrupt (Fig. 15).

Nevertheless, one should bear in mind that the aim is to develop a relatively simple approach using

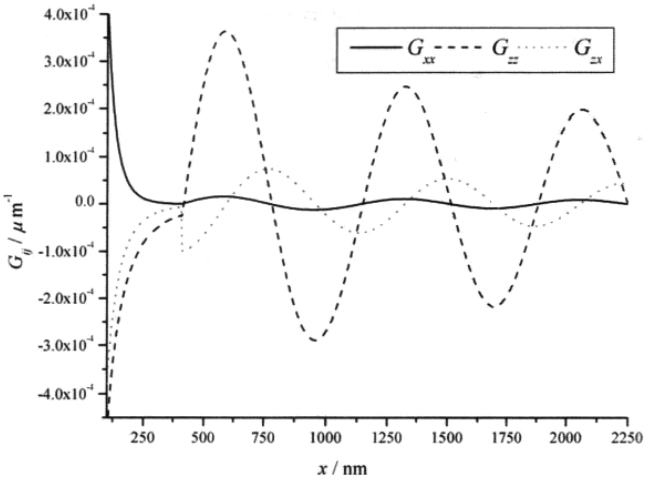

Fig. 15. Nonzero dyadic components calculated at the height of 40 nm above the gold surface for $\lambda_0 = 750$ nm using the near-field and SPP dyadic for distances correspondingly smaller and larger than the transition distance of $3\lambda/5$.

analytic *approximations* of the total Green dyadic, so as to be able of dealing with a complex surface system with many strongly interacting particles. Then, the Green dyadic used in the presented simulations is set to the following form

$$G(r,r') = \begin{cases} G_{nf}(r,r') & \text{for } |r-r'| \le 3\lambda/5\,, \\ G_{\mathrm{SPP}}(r,r') & \text{for } |r-r'| > 3\lambda/5\,. \end{cases} \tag{30}$$

The incident electric field is considered to be formed by an incident (normal to the air-surface interface) Gaussian beam with linear polarization and its reflection by the interface:

$$E^0(r) = e_\rho E^0 \exp\left(-\frac{(x-x_{\mathrm{scan}})^2 + (y-y_{\mathrm{scan}})^2}{w_0^2}\right) \\ * \cdots (e^{ik_0 z} + \gamma e^{-ik_0 z})\,, \tag{31}$$

where E^0 is the field amplitude, the polarization along either $\hat{x}$ or $\hat{y}$ is defined by the vector $e_\rho = (1,0,0)$ or $e_\rho = (0,1,0)$ respectively, the beam center is located at the scanning coordinates (x_{scan}, y_{scan}) and w_0 is the beam radius at the intensity level e^{-1}. Finally, the phase difference between the incident and the reflected fields at the height z above the surface is incorporated by the last term, where $\gamma = (1-n)/(1+n)$ is the reflection coefficient of the gold surface having refractive index $n = \sqrt{\varepsilon}$.

Starting with the incident field as in Eq. (31) and using this field, $E^0(r_i)$, at the centers of all particles, one can proceed solving Eq. (18) with the proper Green dyadic $G(r_i,\, r_j)$ from Eq. (30) and determining the self-consistent fields $E(r_i)$, at the positions of all particles. The FH-SOM image can then be calculated by summing up the scattered fields from all particles and the reflected (by a flat metal surface) incident field at the position of a remote detector. The first contribution is proportional to the sum of the corresponding in-plane fields at the site of the particles[45] weighted with the factor depending on an effective aperture of the detector so as to correctly balance the signals from the reflected Gaussian beam and the scattered fields. The effective factor was selected from the appearance of experimental and simulated images (for the parallel polarization configurations). For example, the intensity in FH-SOM images, for both incident and detected polarizations being parallel to the x-axis, were simulated as follows:

$$I_\omega^{xx}(x_{\mathrm{scan}}, y_{\mathrm{scan}}) = \left|\Gamma E^{\mathrm{refl}} + \sum_i^N E_x(\omega, r_i)\right|^2\,, \tag{32}$$

where

$$E^{\mathrm{refl}} = \gamma e^{-ik_0\alpha} = \frac{1-n}{1+n} e^{-ik_0\alpha}\,. \tag{33}$$

Contain the reflection coefficient and phase used in the last term of Eq. (31). In this case $\Gamma = 100$ was selected in order to obtain qualitative agreement in the image contrast with experimental FH images of random gold nanostructures.[41,44] For the cross-polarized configurations, the reflected incident field is not detected and $\Gamma = 0$ was used.

Simulation of the SH-SOM images is more complicated and requires several calculation steps. The main circumstance to be kept in mind is that, for symmetry reasons, metal does not posses second-order susceptibilities $\chi^{(2)}$ in bulk.[46] SH fields can be therefore generated only at the (flat) metal surface and the scatterers. Though the latter process, occurring insofar spherical particles are being close to the metal surface, is not efficient. In any case, the contribution to SH generation from the z-component (normal to the surface) of the FH field would significantly exceed those from the x- and y-component (parallel to the surface). To simplify the consideration, assume that the main source of SH radiation are the z-components of the SH field at the sites of the particles $E_z^0(2\omega, r_i)$, which are proportional to the SH z-components at the surface driven by the FH z-component at the surface $E_z(\omega, x_i, y_i, z=0)$ and that the latter is proportional to the FH z-component at the sites of the

particles:

$$E_z^0(2\omega, r_i) \propto E_z(2\omega, x_i, y_i, z = 0) \propto E_z^2(\omega, x_i, y_i, z = 0) \propto E_z^0(\omega, r_i)\,. \tag{34}$$

This SH field distribution (at the site of the particles) was then used as an incident SH field $E_z^0(2\omega, r_i)$ in order to determine the self-consistent SH field $E(2\omega, r_i)$ by solving (as in the FH case) the self-consistent equation for SH fields analogous to Eq. (18). The SH-SOM images were simulated similarly to the FH-SOM images by summing up the in-plane components of SH fields. For example, in the case of different polarizations of the incident FH (x-polarization) and detected SH (y-polarization) fields, the SH image was calculated as follows

$$I_{2\omega}^{xy}(x_{\text{scan}}, y_{\text{scan}}) = \left| \sum_i^N E_y(2\omega, r_i) \right|^2 . \tag{35}$$

8.2. *FH and SH-SOM images*

The FH- and SH-SOM images were calculated with the incident field chosen as in Eq. (31), with the beam radius set to $\omega_0 = 0.5\,\mu$m and taken at the centers of the particles ($z = a$). FH and SH images, of a high density sample $50\,\mu\text{m}^{-2}$ of nanoparticles with raidus = 40 nm, were calculated for various polarization configurations at the incident light wavelength of 750 nm (Figs. 16(a)–16(h)). It is seen that the appearance of both FH and SH images is similar to that of experimentally obtained images reported in Ref. 41, with the main feature of occurrence of SH bright spots, whose locations depend on polarization, being clearly reproduced.[41] For the parallel polarization configuration, the lowest signals in the FH images appear inside the area of scatterers, where the incident field is scattered into other polarizations, as opposed to the cross-polarized configurations, where the only nonzero signals appear inside the scattering area. One conspicuous detail about the FH images is that the reversed cross-polarized configurations, i.e., (x, y)- and (y, x)-configurations, result in exactly the same images that are also more sensitive to polarization than the FH images. Such a striking difference is related to the circumstance that the reversed FH images correspond to the reciprocal SOM configurations that should produce the same images,[41,42] whereas the SH images are produced in the process of nonlinear imaging so that the reversed configurations are not reciprocal. It is also seen

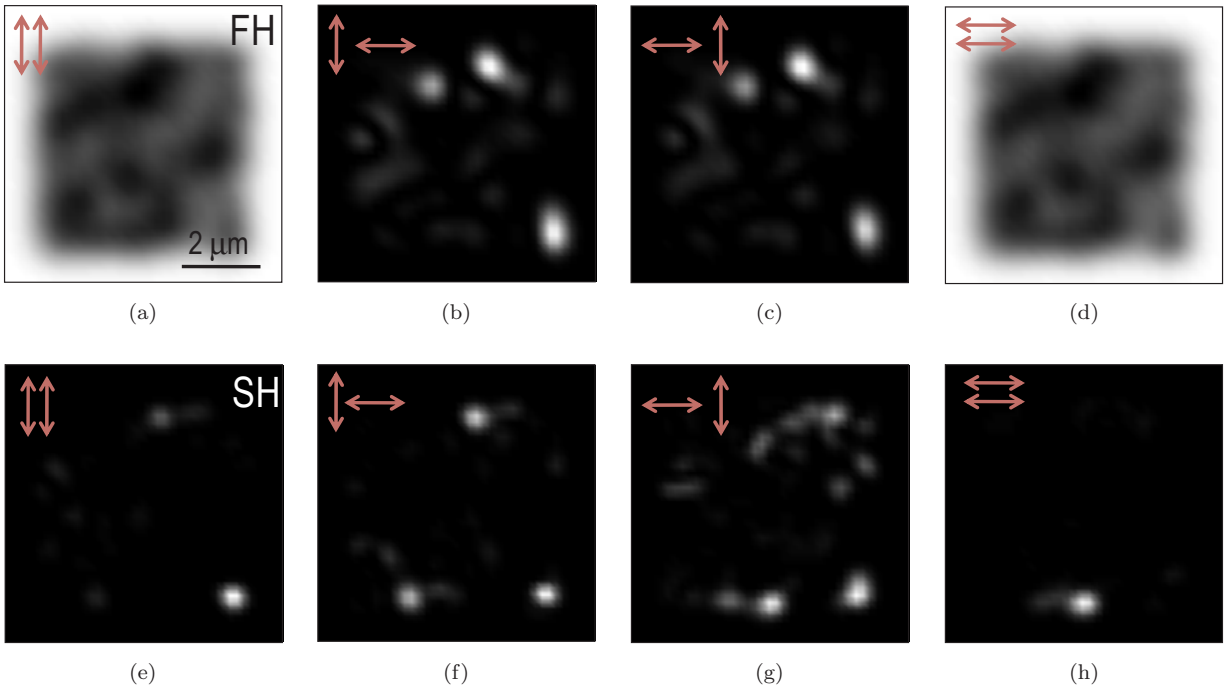

Fig. 16. Intensity distributions maps (a)–(d) FH and (e)–(h) SH images ($7 \times 7\,\mu\text{m}^2$) of a sample with a particle density of 30 particles/μm^2 for the wavelength of 750 nm and the polarization configurations indicated by arrows (excitation — left, detection — right arrow).

that the SH images are considerably more sensitive to the wavelength than the FH images. As was previously suggested, the very bright spots in the SH images could occur due to spatial overlap of properly polarized FH and SH eigenmodes.[41,42] The bright spots in SH images are therefore related to the positions of FH and SH eigenmodes both being sensitive to the wavelength. Consequently; the SH bright spots turn out being more sensitive to the wavelength than the FH bright spots.

9. Outlook

In this paper, the basic fundaments of SPPs along with some results concerning the modeling of plasmonic phenomena were reviewed. Even though in the last years, there has been a great progress in the understanding of plasmonic phenomena, there are no complete theoretical model to deal with such studies. In that context, a relative simple scalar multiple SPP scattering model was presented. Microscatterers were considered in a two-dimensional geometry as isotropic point-like particles characterized by their effective polarizabilities. Different regimes of SPP scattering were numerically simulated in a random distribution of nanoparticles. The corresponding Fourier spectra of the intensity distributions showed distinctly different spectra for each of the calculated regimes. The scalar model has limitations on the accuracy of numerical results. For example, the effective polarizability of an individual particle is a phenomenological quantity that is difficult to relate to particle parameters such as size, susceptibility, etc. The scalar approach was extended into a vectorial dipolar model for SPP multiple-scattering and used to model the operation of a SPP-based beam-splitter and an interferometer whose main element represented individual scatterers lined up and equally spaced. One can try to further improve this model by, for example, developing another (but analytical as well) approximation of the Green's tensor for relatively small inter-particle distances.

We modeled SPP excitation and manipulation by nanoarrays. The feasibility of simultaneous excitation, propagation and manipulation of SPP fields was corroborated. The SPP launching was simulated elucidating the influence of square-shaped nanoarray width. Waveguiding of SPP was studied by using different excitation wavelengths. The results show the feasibility to manipulate SPPs without using external excitation elements as for example an in-coupling ridge. In order to further explore this possibility, further theoretical and experimental works are needed. Finally, we presented SH-SOM simulations on generated sets of randomly distributed spherical nanoparticles. The multiple-scattering between the nanoparticles was established through self-consistent calculations of the electric field distributions using a combination of two separate expressions for the involved Green dyadic, valid either for shorter- or longer-interaction distances. In general, the simulations presented here offered qualitatively good agreement with experimental results,[15,16,22,34,38,41,42] indicating that the approach can be used, with certain limitations, for modeling of plasmonic nanodevices.

Acknowledgment

This project was supported by CONACyT SEP-2004-C01-45999.

References

1. H. Raether, *Surface Plasmons*, Springer Tracts in Modern Physics, Vol. 111, ed. G. Höhler (Springer, Berlin, 1988); *Surface Polaritons*, Modern Problems in Condensed Matter Sciences, Vol. 1, eds. V. M. Agranovich and D. L. Mills (North-Holland, Amsterdam, 1982).
2. R. Zia, J. A. Schuller and M. L. Brongersma, *Mater. Today* **9**, 20 (2006).
3. W. L. Barnes, A. Dereux and T. W. Ebbesen, *Nature* **424**, 824 (2003).
4. T. W. Ebbesen, C. Genet and S. I. Bozhevolnyi, *Phys. Today* **61**, 44 (2008).
5. I. I. Smolyaninov, D. L. Mazzoni and C. C. Davis, *Phys. Rev. Lett.* **77**, 3877 (1996).
6. S. I. Bozhevolnyi and F. Pudonin, *Phys. Rev. Lett.* **78**, 2823 (1997).
7. I. I. Smolyaninov, D. L. Mazzoni, J. Mait and C. C. Davis, *Phys. Rev. B* **56**, 1601 (1997).
8. S. I. Bozhevolnyi, J. Erland, K. Leosson, P. M. W. Skovgaard and J. M. Hvam, *Phys. Rev. Lett.* **86**, 3008 (2001).
9. S. I. Bozhevolnyi, V. S. Volkov and K. Leosson, *Phys. Rev. Lett.* **89**, 186801 (2002).
10. Z. Liu, J. M. Steele, W. Srituravanich, Y. Pikus, C. Sun and X. Zhang, *Nano Lett.* **5**, 1726 (2005).
11. A. Drezet, A. L. Stepanov, H. Ditlbacher, A. Hohenau, B. Steinberger, F. R. Aussenegg, A. Leitner and J. R. Krenn, *Appl. Phys. Lett.* **86**, 074104 (2005).

12. D. S. Kim, S. C. Hohng, V. Malyarchuk, Y. C. Yoon, Y. H. Ahn, K. J. Yee, J. W. Park, J. Kim, Q. H. Park and C. Lienau, *Phys. Rev. Lett.* **91**, 143901 (2003).
13. E. Devaux, T. W. Ebbesen, J.-C. Weeber and A. Dereux, *Appl. Phys. Lett.* **83**, 4936 (2003).
14. A. Drezet, A. Hohenau, A. L. Stepanov, H. Ditlbacher, B. Steinberger, F. Aussenegg, A. Leitner and J. Krenn, *Plasmonics* **1**, 141 (2006).
15. I. P. Radko, S. I. Bozhevolnyi, A. B. Evlyukhin and A. Boltasseva, *Opt. Exp.* **15**, 6576 (2008).
16. I. P. Radko, A. B. Evlyukhin, A. Boltasseva and S. I. Bozhevolnyi, *Opt. Exp.* **16**, 3924 (2008).
17. A. V. Shchegrov, I. V. Novikov and A. A. Maradudin, *Phys. Rev. Lett.* **78**, 4269 (1997).
18. I. I. Smolyaninov, D. L. Mazzoni and C. C. Davis, *Phys. Rev. Lett.* **77**, 3877 (1996).
19. S. I. Bozhevolnyi and F. A. Pudonin, *Phys. Rev. Lett.* **78**, 2823 (1997).
20. I. I. Smolyaninov, D. L. Mazzoni, J. Mait and C. C. Davis, *Phys. Rev. B* **56**, 1601 (1997).
21. F. W. J. Olver, *Handbook of Mathematical Functions*, eds. M. Abramowitz and I. A. Stegun (Dover, New York, 1972), Chapter 9, pp. 355–433.
22. S. I. Bozhevolnyi and V. Coello, *Phys. Rev. B* **58**, 10899 (1998).
23. S. I. Bozhevolnyi and V. S. Volkov, *Opt. Commun.* **198**, 241 (2001).
24. T. Søndergaard and S. I. Bozhevolnyi, *Phys. Rev. B* **67**, 165405 (2003).
25. B. J. Soller and D. G. Hall, *JOSA B* **19**, 2437 (2002).
26. D. A. Genov, A. K. Sarychev, V. M. Shalaev and A. Wei, *Nano Lett.* **4**, 153 (2004).
27. V. Coello, T. Søndergaard and S. I. Bozhevolnyi, *Opt. Commun.* **240**, 345 (2004).
28. A. B. Evlyukhin and S. I. Bozhevolnyi, *Phys. Rev. B* **71**, 134304 (2005).
29. A. B. Evlyukhin and S. I. Bozhevolnyi, *Laser Phys. Lett.* **3**, 396 (2006).
30. T. A. Lesoka, A. A. Maradudin and E. R. Méndez, *Optical Properties of Nanostructured Random Media*, ed. V. M. Shalaev (Springer-Verlag, Berlin, 2002), pp. 359–439.
31. J. Beermann, S. I. Bozhevolnyi and V. Coello, *Phys. Rev. B* **73**, 115408 (2006).
32. F. de Fornel, *Evanescent Waves from Newtonian Optics to Atomic Optics* (Springer-Verlag, GM, 2001).
33. D. W. Pohl, *Near-Field Optics and Surface Plasmon Polaritons*, Topics in Applied Physics, Vol. 81, ed. S. Kawata (Springer, Berlin, 2001), pp. 1–10.
34. V. Coello, S. I. Bozhevolnyi and F. A. Pudonin, Imaging of surface plasmons with a near-field microscope, *Proc. SPIE* **3098**, 536 (1997).
35. S. I. Bozhevolnyi, *Phys. Rev. B* **54**, 8177 (1996).
36. T. Søndergaard and S. I. Bozhevolnyi, *Phys. Rev. B* **69**, 045422 (2004).
37. V. S. Volkov, S. I. Bozhevolnyi, K. Leosson and A. Boltasseva, *J. Microscopy* **210**, 324 (2003).
38. H. Dittlbacher, J. R. Krenn, G. Shider, A. Leitner and F. R. Aussenegg, *Appl. Phys. Lett.* **81**, 1762 (2002).
39. B. J. Soller and D. G. Hall, *JOSA B* **19**, 2437 (2002).
40. D. A. Genov, A. K. Sarychev, V. M. Shalaev and A. Wei, *Nano Lett.* **4**, 153 (2004).
41. S. I. Bozhevolnyi, J. Beermann and V. Coello, *Phys. Rev. Lett.* **90**, 197402 (2003).
42. V. Coello, J. Beermann and S. I. Bozhevolnyi, *Phys. Stat. Sol.* (*C*) **0**, 3070 (2003).
43. O. Keller, M. Xiao and S. I. Bozhevolnyi, *Surf. Sci.* **280**, 217 (1993).
44. J. Beermann and S. I. Bozhevolnyi, *Phys. Rev. B* **69**, 155429 (2004).
45. S. I. Bozhevolnyi and V. Z. Lozovski, *Phys. Rev. B* **65**, 235420 (2002).
46. R. W. Boyd, *Nonlinear Optics*, 1st edn. (Academic Press, UK, 1992).